Numerical Analysis of Heterogeneous Methanol Flames Over Porous Sphere Surfaces Using Short Kinetics Mechanism

Sharanya Nair and Vasudevan Raghavan

1 Introduction

The porous sphere technique is a simplified representation of fuel particle or droplet burning in a forced convective environment. It consists of an experimental setup with a porous sphere placed in an air flow, with fuel being supplied at the center of the sphere at the rate of its consumption in the flame. It is ensured that the entire sphere surface is uniformly wet with the fuel, and dripping of the liquid is avoided. This technique has been often used to examine the mass burning characteristics and chemical structure of flames from various liquid fuels. Two types of flames are observed to be formed based on the convective air velocity; one is an envelope flame, which surrounds the sphere, and the second is a wake flame formed in the wake region of the sphere. In spray combustion, the flames could sustain in the wake of the droplet, when droplet moves with higher velocities from the fuel injector. The flame further transitions into the envelope regime as the droplet decelerates due to drag. Spalding [1] reported a critical velocity for the air flow, at which a flame does not sustain in the upstream face of the sphere. This transitional (critical) velocity, at which there is a rapid reduction in mass loss rate, was seen to be proportional to the sphere diameter [1]. Sami and Ogasawara [2] conducted experiments on porous spheres in a heated (300–900 K) and pressurized (0.4–16 bar) air stream, up to the transitional velocity to wake regime. The mass burning rate was seen to increase significantly with pressure and temperature. The high temperature was found to increase the transitional velocity. Gollahalli and Brzustowski [3] further verified the envelope and wake regimes of flames around porous spheres. König et al. [4] presented the structure of the flame

S. Nair (✉)
Worcester Polytechnic Institute, Worcester, MA 01609, USA
e-mail: snair2@wpi.edu

V. Raghavan
Indian Institute of Technology Madras, Chennai, Tamilnadu 600036, India

N. L. Narasimhan et al. (eds.), *Recent Advances in Energy Technologies*, Lecture Notes in Mechanical Engineering, https://doi.org/10.1007/978-981-19-3467-4_32

over fuel fed porous sphere by measuring OH radical using Laser Induced Predissociation Fluorescence (LIPF) under micro-gravity conditions. Experimental and numerical studies on mass burning rates and flame shapes around fuel fed porous spheres were reported by Balakrishnan et al. [5]. The effects of air velocity on burning porous sphere in upward and downward configurations were analyzed, and the flame shapes and mass loss rates were reported. A numerical model with constant properties (excluding density) and infinite rate kinetics was used to simulate the experimental cases. A flattened flame front was seen for higher downward velocity, which opposed the natural convection. Raghavan et al. [6] conducted experimental and numerical studies on porous spheres in convective air to identify these two flame regimes. For the numerical model, a global single-step reaction with finite rate kinetics was used along with varying thermo-physical properties, to analyze the flame shape and mass burning rates in envelope and wake flame regimes. The predicted results were reasonably close to the experimental data in the envelope flame regime [6]. Transition velocity and wake flame features were predicted by finite rate chemistry, but not with infinite rate chemistry. An experimental study using porous sphere technique was recently conducted by Das et al. [7] to study the mass loss rate variation and transition from envelope flame to wake regimes under atmospheric conditions. A theoretical model considering mixed convective transport for mass burning rate was validated for methanol. A power law for dimensionless mass burning rate was proposed with respect to the effective Reynolds number.

Literature survey portrays that experimental results are available for burning of liquid methanol fuel over porous sphere surfaces in convective environment, in terms of flame shapes and mass burning rates in both envelope and wake regimes. The numerical models in literature have incorporated infinite rate chemistry or a global single-step reaction kinetics to model oxidation of methanol. This is sufficient to bring out the characteristics of envelope flames under different conditions, which are non-premixed flames, controlled by transport processes. However, a single-step reaction kinetics are not accurate enough to predict the characteristics of a wake flame, which is a partially premixed flame. Intermediate species and radicals, and elementary reactions involving them, are required for this purpose. Therefore, at least a short kinetics mechanism with sufficient number of species and elementary reactions is required for analysis of the flame shape and mass burning rates. Such a mechanism is reported in Tarrazo et al. [8], and this is used to validate various types of homogeneous and heterogeneous flames by Nair and Raghavan [9]. In this study, heterogeneous methanol flames over single and two porous spheres are simulated using this numerical model [9]. Detailed analysis of the characteristics of envelope and wake flames is reported. Interference effects between two equal and unequal spheres burning one over the other are also studied.

2 Numerical Methodology

Numerical simulations are performed using a pressure-based axisymmetric (r-x coordinates) solver in Ansys Fluent. A short chemical mechanism [8] with 18 species (CH_3OH, O_2, O, H, OH, H_2, H_2O, HO_2, H_2O_2, CO, CO_2, HCO, CH_3, CH_4, CH_2O, CH_3O, CH_2OH, and N_2) and 38 elementary reactions is implemented to model the methanol oxidation. To consider radiation losses due to species such as CH_4, CO_2, CO, and H_2O, an optically thin radiation model [10] is incorporated in the energy equation as a negative source term using a user-defined function (UDF). Variable thermo-physical properties and full multi-component diffusion including Soret effect are included. In experiments, since methanol is fed at the rate at which it is consumed, the flames are quasi-steady in nature. For flames over a condensed fuel surface, interface coupling conditions are prescribed at the sphere surface and only the gas-phase is solved.

A non-reactive cold flow simulation is executed for a low air velocity of 0.4 m/s. The convergence criteria are set as normalized values for the residuals less than 10^{-3} for continuity and 10^{-4} for momentum and species equations. After convergence, a small region near the front stagnation point of the sphere is initialized with a temperature of 1500 K and volumetric reactions are enabled. Energy equation and volumetric reactions are solved with convergence criterion of normalized energy residual to be less than 10^{-6}. Moreover, normalized mass imbalance ratio of net outgoing flow to the lowest incoming mass flow rate is ensured to be less than 1%. Similarly, it is ensured that the normalized heat imbalance is less than 5%. In the case where the flow is transient, unsteady cases are executed with the time step of 10^{-5} s, providing adequate iterations within the time step to converge these equations. Air inlet velocity is changed in small increments of 0.2 m/s, and converged reactive solutions are obtained for each velocity.

2.1 Computational Domain and Grid Independence

The computational domains are shown in Fig. 1a, b, for single and two porous spheres, respectively. Here D is diameter of the porous sphere and S is the spacing between the centers of the two spheres. Ambient air enters through the air inlet at a uniform velocity.

At the surface of a porous sphere, coupled interface conditions are used based on the energy balance and mass and momentum conservation. In Ansys Fluent, these are defined using a user-defined function (UDF) with latent heat of vaporization (h_{fg}) and the temperature-dependent properties of mixture density (ρ), mixture thermal conductivity (k), and binary mass diffusion coefficient, being the input parameters at the boundary. The detailed explanation of the coupled interface boundary condition including the equations has been listed below.

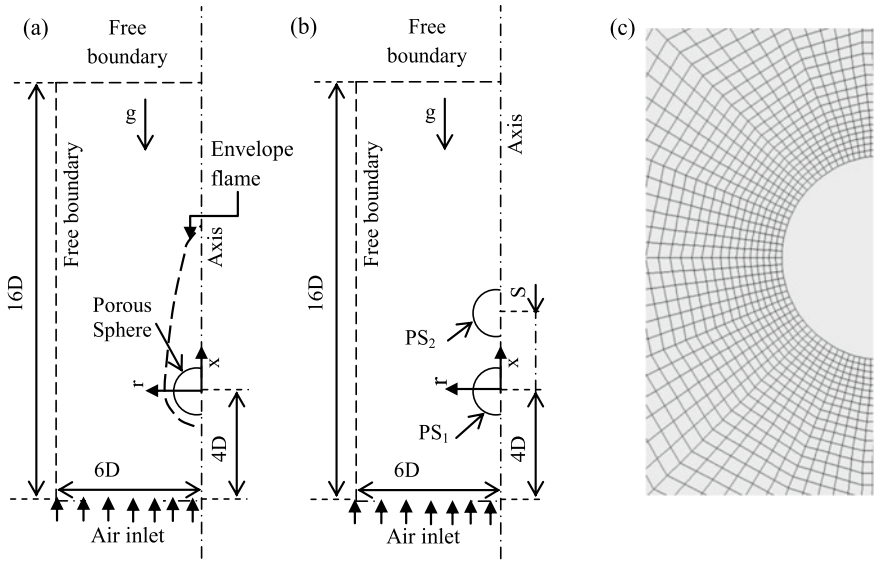

Fig. 1 Computational domain for **a** single porous sphere, **b** two porous spheres, and **c** structured, multi-block mesh near the porous sphere surface

(i) Heat transfer by conduction from the ambient to the sphere surface is considered for calculating the liquid surface temperature, T_s (surface denoted by subscript s). The heat addition to the sphere surface due to radiation has not been considered following literature [6, 11]. The energy conservation at the interface can be written by equating the product of mixture density, ρ, normal component of velocity, v, and latent heat of vaporization of the liquid fuel, h_{fg} to the product of the normal temperature gradient at the surface and mixture thermal conductivity, λ as shown in Eq. (1). Thus, for steady equilibrium evaporation,

$$\rho_s v_s h_{fg} = \lambda_s \left.\frac{\partial T}{\partial n}\right|_s \tag{1}$$

Here, subscript s denotes the interface quantity. Using a 3-point interpolation, the temperature gradient is evaluated using surface temperature of the fuel and temperature values in two adjacent interior nodes.

(ii) The partial pressure, p in mm Hg, of the methanol vapor above the fuel surface is calculated as the saturation pressure at the surface temperature using the Antoine equation. Including methanol specific constants [12], $A = 8.08097$, $B = 1582.27$, and $C = 239.7$, the Antoine equation is written as,

$$\log_{10} p = A - B/(C + T_s - 273.15) \tag{2}$$

From the partial pressure (or the mole fraction) of the species, its molecular mass, and the mixture molecular mass, the mass fraction of fuel denoted as Y_F can be calculated.

(iii) The mass flux of the fuel due to evaporation is evaluated from Fick's law of ordinary diffusion as shown in Eq. (3). It considers the molecular diffusion between the fuel vapor and nitrogen, D_{Fs}, and the gradient of fuel mass fraction at the interface normal to the sphere surface. A 3-point interpolation is used to evaluate this derivative of mass fraction of the fuel at the surface.

$$\rho_s v_s = \rho_s v_s Y_{Fs} - \rho D_{Fs} \left.\frac{\partial Y_F}{\partial n}\right|_s \tag{3}$$

(iv) Using Fick's law, the mass fractions of all other species, denoted as Y_i, are calculated such that each of their net mass flux at the interface is zero. This is written as,

$$\rho_s v_s Y_i = \rho D_{is} \left.\frac{\partial Y_i}{\partial n}\right|_s \tag{4}$$

Again, 3-point interpolation is used to calculate the derivative of mass fraction of species i at the interface normal to the surface. For species i, the binary diffusivity with respect to its diffusion with nitrogen, D_{is}, is calculated using Lennard–Jones parameters at the surface temperature, T_s. These equations are solved iteratively within a main iteration so that the output values of T_s, v_s, Y_{Fs}, and Y_{is} at all the nodes of the interface converge to required accuracy (normalized difference between two inner iterations for each variable is within 0.1%).

The free boundaries in the domain are pressure-specified. When the flow goes out of the computational domain, the variables are extrapolated from the interior. If due to adverse pressure gradient, the flow comes into the domain, then ambient air (21% O_2 and 79% N_2) at 300 K is assumed to enter the domain.

Structured, multi-block, and quadrilateral cells have been used to divide the domain in a nonuniform manner, as shown in Fig. 1c, maintaining orthogonality of the grids at the sphere surface and boundaries. Grid independence study has been done. For the single porous sphere case, coarse (7774 cells), intermediate (10,558 cells) and fine (15,857 cells) meshes are used for free stream velocity of 0.4 m/s.

The profiles of temperature at $r = 0$ and mass fraction of oxygen and carbon-dioxide at $x = 0$ are used as the criteria and have been compared for the three meshes as shown in Fig. 2. It is seen in Fig. 2 that the profiles almost coincide as grids are refined, with the maximum normalized difference in temperature being about 2% and in mass fraction being about 2.2% and 4.2%, for O_2 and CO_2, respectively between the intermediate and fine grids. The differences between prediction by the three meshes at other axial and radial locations are seen to be smaller. Therefore, the intermediate grid has been used for the analysis.

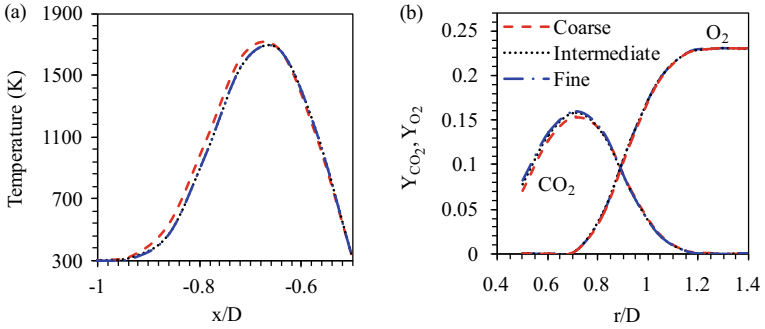

Fig. 2 Grid independence check in terms of profiles of **a** temperature at $r = 0$ and **b** mass fraction at $x = 0$

2.2 *Numerical Model Validation*

The numerical model is validated for single porous sphere of diameter 8 mm, for which experimental data is available [6, 7]. The effects of varying the air velocity from 0.4 m/s to 1.6 m/s on the mass burning rate and the flame stand-off are shown in Fig. 3a and b, respectively. The mass burning rate is evaluated as an area integral of the mass flux along the entire sphere surface. The flame stand-off distance is evaluated as the distance from the location of the stoichiometric oxygen to methanol ratio at the axis measured from the front stagnation point of the sphere. The stoichiometric oxygen to methanol ratio is calculated from mass fractions (Y) as $Y_{\text{methanol}} - Y_{\text{oxygen}}/\nu = 0$, where ν kg represents the mass of oxygen required to burn 1 kg of methanol.

For the air velocity less than 1.25 m/s, a flame envelopes the sphere. In this range, with increase in air velocity, the flame stand-off is seen to move closer to the sphere surface. As the free stream velocity is further increased to a critical value (predicted as 1.25 m/s for 8 mm sphere diameter), the reaction zone moves downstream of the

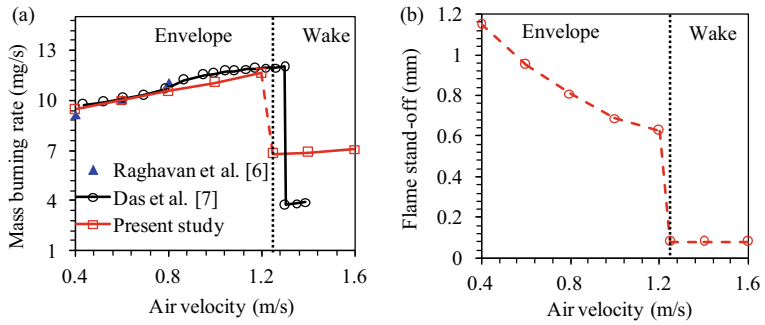

Fig. 3 Variation of **a** predicted and measured mass burning rate and **b** predicted flame stand-off with air velocity for a sphere of 8 mm diameter; vertical line indicates transition from envelope to wake flame regime

sphere to sustain as a wake flame. The value for critical velocity is fine-tuned by reducing the air velocity increment from 0.2 m/s to 0.05 m/s.

The flame in the front portion of the sphere extinguishes due to insufficient flow residence time (Damköhler number (Da) < 1). Damköhler number is defined as the ratio of flow residence time to the chemical reaction time. The flow residence time is obtained by dividing the porous sphere diameter with the free stream air velocity. The chemical reaction time is evaluated as the ratio of concentration of the fuel to its kinetic rate. Even though fuel and oxygen are available near the front stagnation region, reactions occur only in the wake region, where sufficient time is available for them to complete. The case of envelope flame represents diffusion mode of combustion. The rate at which fuel and air mixes determines formation of the flame zone. However, the case of wake flame is like a partially premixed flame, where methanol vapor and air premix around the front stagnation point. The critical air velocity, measured by the experimental study of Das et al. [7] is 1.3 m/s and the numerical model is able to predict this as 1.25 m/s. A lower critical velocity of around 0.9 m/s has been reported for 8 mm sphere in Raghavan et al. [6] even though the mass burning rates in the envelope regime (air velocity < 0.9 m/s) reported by Raghavan et al. [6] are quite closer to those reported by Das et al. [7] (Fig. 3a).

At sub-critical air velocities, where an envelope flame is seen, the mass burning rate (MBR) increases with an increase in the free stream velocity (Fig. 3a). There is a gradual decrease in the flame stand-off distance (Fig. 3b) in the envelope regime due to increased strain caused by the increasing momentum of incoming air near the front stagnation region. At the critical velocity of 1.25 m/s, a wake flame is formed in the rear half of the sphere and a rapid reduction in the mass burning rate is observed when this transition occurs. The location of stoichiometric oxygen to methanol ratio coincides almost with the surface at the front portion of the sphere, indicating no reaction in its front part. The flame stand-off rapidly decreases to a value close to zero (Fig. 3b). As a result of sudden reduction in the flame surface area, a drastic reduction in heat transfer to the sphere surface occurs. Thus, the mass burning rate rapidly decreases as shown in Fig. 3a. The trend and the values of MBR closely follow the experimental values of Raghavan et al. [6] and Das et al. [7]. The wake flame burning rate is over-predicted since it is much difficult to measure the burning rate of wake flames due to the oscillatory nature of the flame and the difficulty in maintaining uniformly wet surface precisely. However, as the transition is predicted well, the results are considered as useful qualitative data. Dynamics of wake flame in the gas-phase, predicted by the model are also quite useful in understanding the nature of partial premixed flames. It was noticed that the rapid decrease in the value of MBR during transition to wake flame and the MBR variation with air velocity in the wake flame regime has not been predicted well by the single-step chemistry [6].

3 Results and Discussion

3.1 Flames Over Single Porous Sphere

An analysis of flames over single 8 mm porous sphere is presented in this section. The temperature contours along with mixture velocity vectors is illustrated in Fig. 4 for four air velocities. Two envelope flames, at air velocities of 0.4 m/s and 1.2 m/s, and two wake flames at air velocities of 1.25 m/s and 1.6 m/s, have been analyzed. The diffusion fluxes of CH_3OH and O_2, as evaluated from ordinary and thermal diffusion, are shown in Fig. 5, along with the contour line of stoichiometric oxygen to methanol ratio. For an 8 mm sphere, the critical velocity is 1.25 m/s. At a velocity slightly lesser than this, say at 1.2 m/s, a clear envelope flame is formed. For 0.4 m/s and 1.2 m/s, as shown in Fig. 4a and b, respectively, an envelope flame is present over the sphere, because sufficient residence time is available for the reactions to complete in the front part of the sphere. The flow is found to curve around the sphere, and it accelerates across the flame zone. As the air velocity is increased within the critical limit, high temperature zone moves closer to the rear portion of the sphere surface, as observed by the isotherm of 1400 K. Around the front stagnation region, the temperature gradient increases due to increased momentum of the incoming air. The maximum temperature in the front stagnation region decreases as a result of higher air velocity that causes convective cooling of the flame. However, the isotherm of 1400 K has come much closer to the front stagnation point, indicating more heat transfer to the sphere surface.

In Fig. 5a, b, for envelope flame cases, fuel vapor and oxygen diffuse into the combustion zone across the stoichiometric contour line, slightly upstream of $x = -0.5D$, to mix and react. At the front stagnation point, the scenario is equivalent to that of an opposed flow flame, where the fuel vapor and air flow in direction opposite to each other. A nonlinear variation of mass flux is observed along the surface of the sphere depending on the flame stand-off distance from the fuel surface, as indicated by the diffusion fluxes. For an envelope flame, the mass flux is the highest at the front stagnation point, due to the availability of fresh air and the presence of highest gradients in that location. The fuel diffusion flux reduces along the sphere surface. The diffusion fluxes are seen to be larger for 0.8 m/s due to higher gradients caused by lower flame stand-off. The stoichiometric contour line shifts toward the front stagnation point as the free stream velocity is increased in the envelope flame regime. These result in an increasing trend of mass burning rate as the free stream velocity is increased (Fig. 3a) in the envelope flame regime.

As the fuel and air velocities are increased, the flame zone becomes thinner due to increased strain rate at the front stagnation point. At the critical air velocity, the strain rate attains a critical value. As a result, the flame extinguishes in the front portion, forming a wake flame (Fig. 4c,d). At 1.25 m/s, when a wake flame sustains in the rear half of the sphere, there is a rapid reduction in the mass loss rate, as shown in Fig. 3a. The stoichiometric contour line almost coincides with the surface at the front portion of the sphere (Fig. 5c,d). In a wake flame, fuel vapors produced in small quantities

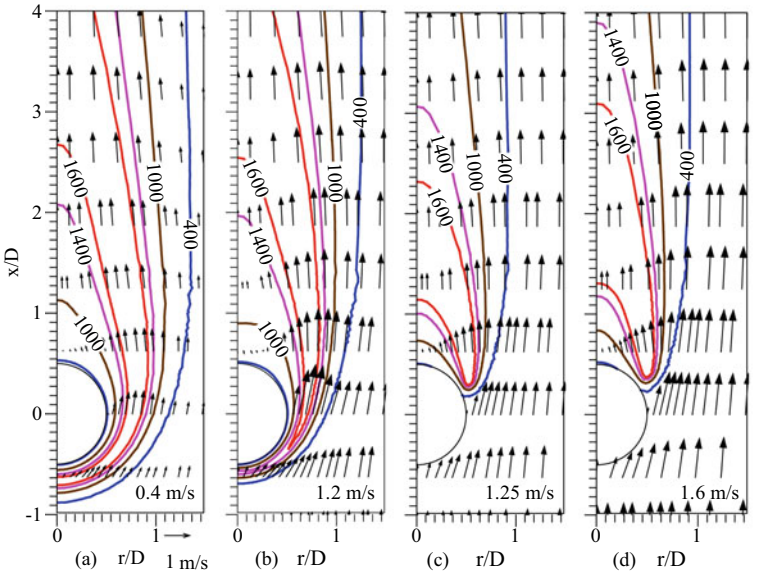

Fig. 4 Temperature contours with mixture velocity vectors for air velocity of **a** 0.4 m/s, **b** 1.2 m/s, **c** 1.25 m/s, and **d** 1.6 m/s; maximum temperature in the domain are **a** 1816 K, **b** 1779 K, **c** 1846 K, and **d** 1934 K

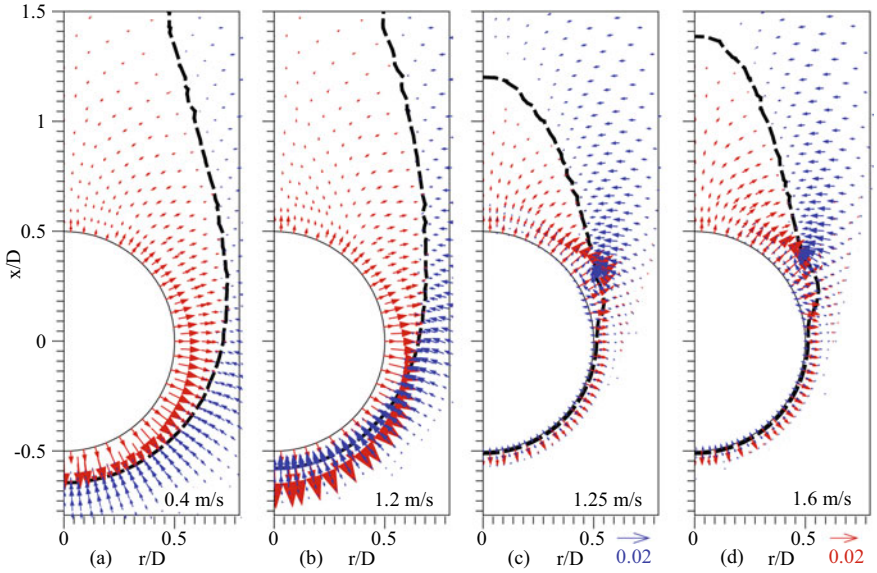

Fig. 5 Stoichiometric contour line (dash line) with vectors of diffusion fluxes (in kg/m^2-s) of CH_3OH and O_2 for air velocity of **a** 0.4 m/s, **b** 1.2 m/s, **c** 1.25 m/s, and **d** 1.6 m/s

in the front part of the sphere are transported to the wake region by the convective air. This results in partial premixing of the reactants. As the free stream velocity is increased in the wake flame regime, the extents of maximum temperature increase, and the flame radius also slightly increases, as shown by the isotherms of 1600 K and 1000 K, in Figs. 4c,d. In Fig. 5c,d, oxygen penetration and partial premixing are observed around $x = 0.25$D, where the flame base sustains. The highest mass flux is located somewhere in the rear half of the sphere, around the flame base. It is also clear that the fuel vapor diffusion occurs at a lower rate in wake flames and the fuel evolved in the front portion of the sphere is carried toward the rear portion as indicated by the mixture velocity vectors, where it burns.

In Fig. 6, contours of the net consumption rate of CH_3OH (kg/m^3-s) are shown in grayscale along with line contours of H_2O and OH mass fractions, for the four air velocities. In Fig. 6a,b, the H_2O mass fraction lines of 0.13 envelope the sphere, and the major fuel consumption zone is visible near the front stagnation of the sphere. The maximum rate of consumption of CH_3OH increases from 31 kg/m^3-s to 55 kg/m^3-s, when air velocity is increased from 0.4 m/s to of 1.2 m/s.

Reaction rate being dependent on the concentrations, due to increased concentrations of methanol vapor (higher burning rate) and oxygen (higher air velocity), a higher consumption rate of CH_3OH is observed. Two pathways for H_2O formation from CH_3OH and OH are

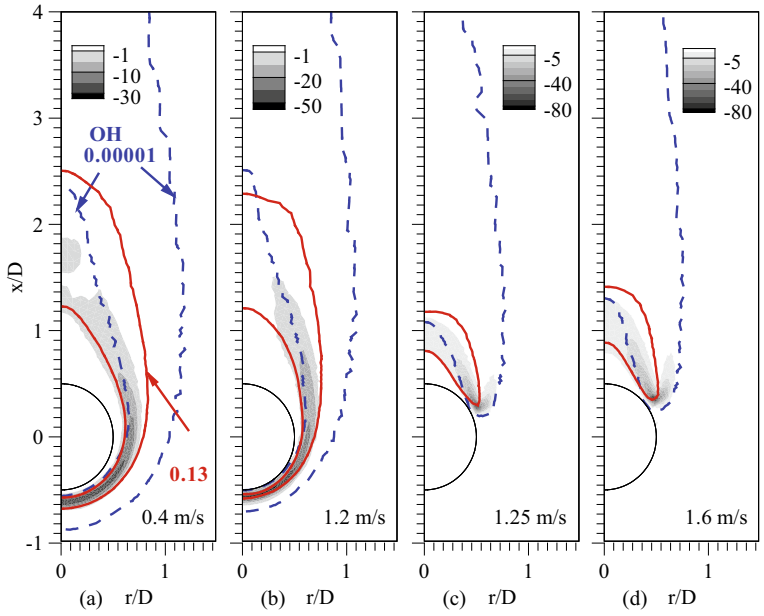

Fig. 6 Contours of net kinetic rate of CH_3OH (negative indicates consumption) with mass fraction lines of OH (dash line) and H_2O (solid line) at **a** 0.4 m/s, **b** 1.2 m/s, **c** 1.25 m/s, and **d** 1.6 m/s

$$CH_3OH + OH \Leftrightarrow CH_2OH + H_2O$$
$$CH_3OH + OH \Leftrightarrow CH_3O + H_2O.$$

These equations are included in the short mechanism. The inner OH mass fraction line with a much low value of 0.00001, which shows its consumption, delineates the consumption rate of CH_3OH to form H_2O in the region. The reaction zone is bound by H_2O mass fraction contour line of 0.13, showing its formation in this region. The OH and H_2O mass fraction lines are seen to shift closer to the sphere surface, at higher air velocity.

At 1.25 m/s, in the wake flame regime, the net consumption rates of CH_3OH along with line contours of mass fractions of H_2O and OH are as shown in Fig. 6c,d. Clearly, the consumption of methanol occurs only in the wake region, although some amount of methanol vapor forms the front portion of the sphere to mix with air. In Fig. 6c,d, two clear branches of methanol consumption are observed. One, branching radially inwards, corresponds to the non-premixed combustion, where the additional methanol vapor from the rear sphere surface mixes with oxygen and burns. The other corresponds to the combustion of partially premixed methanol vapor and air transported from the front part of the sphere. Due to the higher air velocity, the partially premixed mixture is able to burn only at the wake region, where Damköhler number is close to unity. The consumption of OH, as shown by the inner mass fraction line with a value of 0.00001, coincides with the CH_3OH consumption zones. The maximum consumption rate of methanol has increased to 84 kg/m^3-s. This is due to effect of partial premixing in the front portion of the sphere.

3.2 Flames Over Two Porous Spheres in Tandem Arrangement

Interaction of flames from multiple porous sphere surfaces presents interesting features and can reveal the capability of the numerical model with short reaction mechanism to predict such flame interactions. For this, three case studies have been carried out for flames over two porous spheres of: (case 1) equal diameter ($D_1 =$ 8 mm, $D_2 = 8$ mm, and $S = 2D_1 = 16$ mm), (case 2) unequal diameter ($D_1 = 4$ mm, $D_2 = 8$ mm, and $S = 2D_2 = 16$ mm), and (case 3) unequal diameter ($D_1 = 8$ mm, D_2 $= 4$ mm, and $S = 2D_1 = 16$ mm). Here, D_1 and D_2 represent the diameters of porous spheres, PS_1 and PS_2, respectively [Fig. 1b]. Considering integer multiples of the sphere diameter, separation distance of 2D creates maximum interference, without making the spheres touch each other.

For free stream velocity of 0.4 m/s, the contours of temperature (lines) and OH mass fraction (grayscale) along with mixture velocity vectors are illustrated in Fig. 7 for two spheres burning in the envelope flame regime. For the same cases, line contours of oxygen mass fraction and stoichiometric contour line (dashed line) are shown in Fig. 8. When a larger or equal-sized sphere burns in the bottom, a single

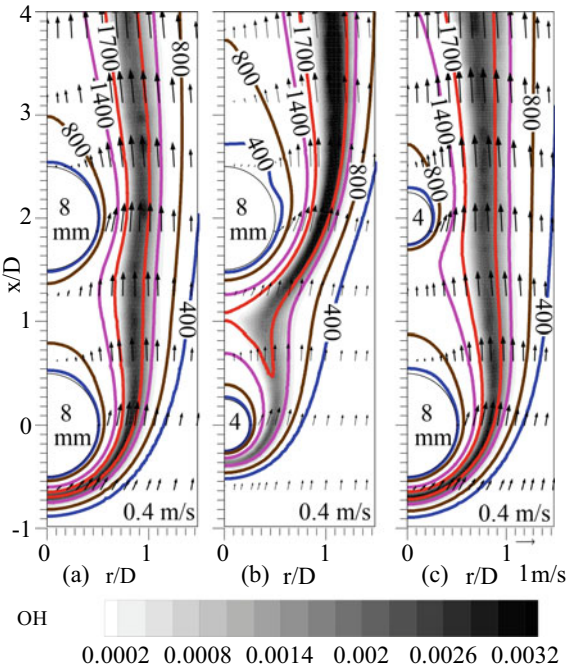

Fig. 7 Temperature and OH mass fraction (grayscale) contours with mixture velocity vectors for air velocity of 0.4 m/s for the case of **a** 8 mm–8 mm, **b** 4 mm–8 mm, and **c** 8 mm–4 mm

envelope flame is observed around the two spheres as indicated by the 1400 K isotherms in Fig. 7a,c and the stoichiometric contour lines in Fig. 8a,c. The mixture velocity vectors are seen to accelerate across the flame (high temperature) zone due to the buoyancy. For the top sphere, it is clear that oxygen is unable to reach its front portion, as indicated by oxygen contour line of 0.02. This is the reason for the absence of individual envelope flame in the top sphere.

In the case of smaller sphere (4 mm diameter) burning at the bottom (Fig. 7b), distinct 1400 K isotherms are observed slightly upstream of the front face for both top and bottom spheres. Deeper oxygen penetration in the wake of the bottom 4 mm sphere is shown by the oxygen contour line of value 0.02 (Fig. 8b). Also, a high temperature zone of 1700 K is clearly visible (Fig. 7b) in between the two spheres, around $x = 1D$, indicating the presence of individual envelope flames around the two spheres. This is ascertained by the stoichiometric contour line in Fig. 8b, which shows that stoichiometric mixing happens in the front face of the 8 mm sphere, in the wake of the 4 mm sphere. The stand-off distances of stoichiometric lines at the front stagnation point for unequal spheres are lesser than that in the equal spheres.

In the envelope flame regime, the mass burning rate (MBR) of the bottom sphere (PS_1) increases with the air velocity, as shown in Fig. 9a–c, because of the movement of the high temperature zone closer to the front stagnation point of the bottom sphere, enhancing the heat and mass transfer processes, like in the isolated sphere case. The trend for flame stand-off location, as evaluated from the location of the stoichiometric line with respect to the front stagnation point of the bottom sphere, shows a gradual

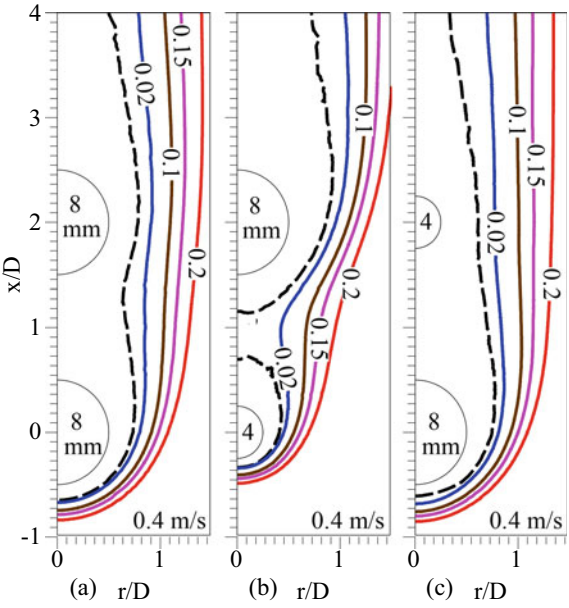

Fig. 8 Oxygen mass fraction contours with stoichiometric line (dash line) for air velocity of 0.4 m/s for the case of **a** 8 mm–8 mm, **b** 4 mm–8 mm, and **c** 8 mm–4 mm

decrease with an increase in the air velocity (Fig. 9d). MBR (Fig. 9a) and flame stand-off (Fig. 9d), in the bottom sphere for 8 mm–8 mm (case 1), are seen to almost coincide with those of the single sphere case, until the transition occurs for the single sphere case. The presence of equal diameter sphere in its wake does not interfere with the flow field in the front part of its surface. For the bottom sphere in 4 mm–8 mm (case 2), shown in Fig. 9b, MBR of the bottom 4 mm sphere (PS_1) is lower than that of the isolated 8 mm sphere, because of its smaller surface area. MBR is seen to increase slightly with an increase in the air velocity until the transition occurs.

For the 8 mm–4 mm (case 3), the variation trend of MBR of bottom 8 mm sphere is similar to that of the single sphere. However, the presence of the smaller sphere in the wake of the larger sphere leads to a flow field that facilitates higher rate of burning (Fig. 9c) for the 8 mm sphere burning at the bottom, when compared to that of the isolated 8 mm sphere. The flame stand-off at each air velocity is seen to be lower for this case as compared to the single sphere case (Fig. 9d).

In the envelope flame regime of the bottom sphere, the mass burning rates of the top spheres are discussed subsequently. The 8 mm sphere at the top in case 1 burns almost like a single sphere having only a wake flame over its rear surface (Fig. 9a). This is because of non-availability of oxygen to its front portion. For 4 mm–8 mm (case 2), MBR is comparable to that of an isolated 8 mm sphere. It has a higher value at 0.4 m/s as compared to that at 0.6 m/s (Fig. 9b). This is due to the presence of individual envelope flames for the two spheres ensuring high temperature gradient near the front face of the top sphere at the velocity of 0.4 m/s. MBR slightly decreases at 0.6 m/s because of the formation of single flame front around both spheres. MBR beyond free stream velocity of 0.6 m/s is seen to almost overlap with that of the single sphere

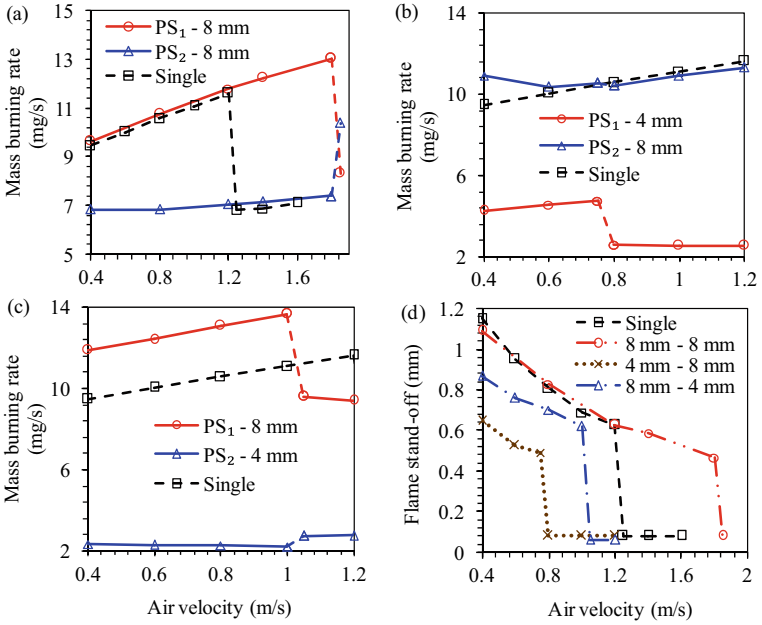

Fig. 9 Mass burning rate variation with air velocity for the case of **a** 8 mm–8 mm, **b** 4 mm–8 mm, **c** 8 mm–4 mm, and **d** flame stand-off variation with air velocity for the bottom sphere

case, indicating lesser interference from the small flame over the smaller sphere at the bottom. For the top sphere in 8 mm–4 mm (case 3), the mass burning rate is much lower (Fig. 9c), since it has a smaller diameter (smaller surface area), and it burns in the wake region of the 8 mm sphere that shadows the incoming flow field with fresh oxygen.

Due to the presence of either an equal or an unequal sphere at the wake region, transition to wake flame occurs for the bottom sphere at a different air velocity when compared to that of isolated sphere case. In the wake regime, contours of temperature (lines) along with mixture velocity vectors and OH mass fraction (grayscale) at the critical velocity for each of the two sphere cases are shown in Fig. 10.

The oxygen mass fraction contour lines and the stoichiometric line (dashed line) for the same cases are portrayed in Fig. 11. For 8 mm–8 mm (case 1), transition to wake flame occurs at a critical velocity of 1.85 m/s (Fig. 10a), which is notably higher than the isolated sphere (1.25 m/s). Isotherm of 1700 K, bounding the OH mass fraction contours, is observed close to the top sphere. As opposed to the wake flame in the single sphere (Fig. 4c), the wake flame in this case sustains at a location farther from the rear point of the bottom sphere, due to higher air velocity that pushes the flame zone further downstream. Due to the occurrence of flame transition for the bottom sphere, oxygen penetration is observed near the front half of the top sphere indicating the formation of the flame zone. Thus, its MBR increases rapidly as shown in Fig. 9a.

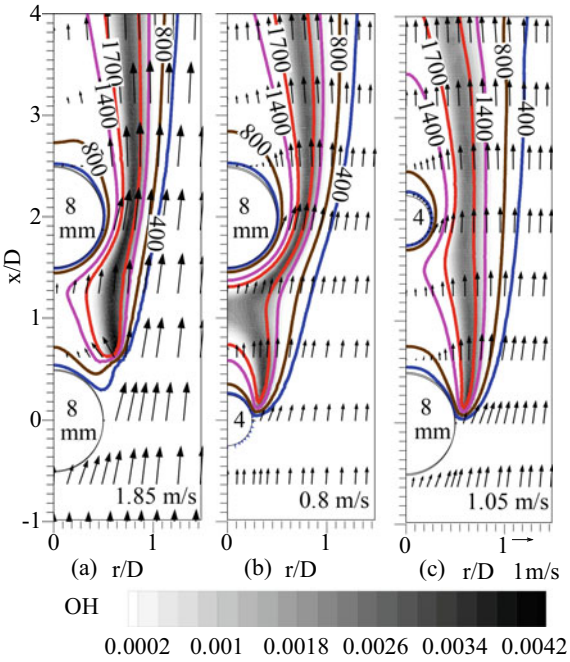

Fig. 10 Temperature and OH mass fraction (grayscale) contours with mixture velocity vectors at critical velocity for the case of **a** 8 mm–8 mm, **b** 4 mm–8 mm, and **c** 8 mm–4 mm

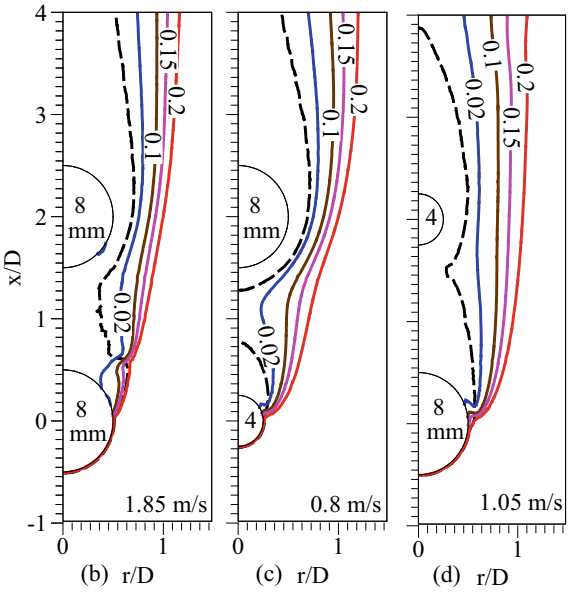

Fig. 11 Oxygen mass fraction contours with stoichiometric line (dash line) at critical velocity for the case of **a** single sphere, **b** 8 mm–8 mm, **c** 4 mm–8 mm, and **d** 8 mm–4 mm

At 0.8 m/s, for 4 mm–8 mm (case 2), transition occurs for 4 mm sphere burning at the bottom. Critical velocity of transition is dependent on sphere diameter and interference effects. An individual envelope flame is seen around the top 8 mm sphere. The wake flame of the bottom sphere just merges with the base of the envelope flame over the top sphere in the spacing between the two spheres, as denoted by the OH mass fraction contours and 1700 K isotherm (Fig. 10b). This is also indicated by distinct stoichiometric lines for bottom and top spheres in Fig. 11b. In the wake flame, oxygen penetration is seen near $x = 0.2D$, as shown by oxygen mass fraction line of 0.02. The stoichiometric line is seen to move closer toward the top sphere with an increase in air velocity from 0.4 m/s (Fig. 8b) to 0.8 m/s (Fig. 11b). As a result, MBR increases with air velocity for the top sphere (Fig. 9b), comparable to that of the isolated sphere, with a least interference from the smaller sphere burning in wake regime at the bottom.

The transition to the formation of a wake flame for the bigger sphere at the bottom is delayed in 8 mm–4 mm (case 3) and occurs at 1.05 m/s (Figs. 10c and 11c), as opposed to the case 2. However, this is a lower velocity when compared to that of the single sphere case. At 1.05 m/s, a single flame front is observed in the wake regime of the bottom sphere, enveloping the top sphere, as portrayed by the OH mass fraction contours and the stoichiometric line in Fig. 10(c). Oxygen penetration is observed near $x = 0.25D$ for the bottom sphere following the O_2 mass fraction line of 0.02 in Fig. 11c. Individual envelope flame does not form around the 4 mm sphere in the wake regime due to oxygen starvation, unlike the wake flame shown in Fig. 11b.

At the critical velocity, there is a rapid decrease in the flame stand-off distance (Fig. 9d) due to absence of the flame in the front half of the bottom sphere. MBR of the bottom sphere reduces rapidly (Fig. 9a–c). For the top sphere, there is an increase in MBR with the air velocity, after the occurrence of wake flame transition in the bottom sphere, due to an increased oxygen penetration to the front portion of the top sphere and existence of high temperature zone near that region as shown in Figs. 10 and 11. Reaction zones are analyzed subsequently (Fig. 12).

The net consumption rate of O_2 in kg/m^3-s is shown as grayscale contours in Fig. 12, for envelope flame cases, at an air velocity of 0.4 m/s. CO_2 primarily forms from OH through the chain propagation reaction,

$$CO + OH \Leftrightarrow CO_2 + H$$

The mass fraction contour line of CO_2 that branch out from the maximum consumption zone of O_2 has a value of 0.14. This shows the bounds where CO_2 is formed. Similarly, OH mass fraction lines of 0.00001 (low value) bound the O_2 consumption zone. Major oxygen consumption is observed near the front stagnation of the bottom sphere for all the cases. A single continuous consumption zone for O_2 around both the spheres is seen Fig. 12a and c, due to shadowing of the incoming air flow by the bottom 8 mm sphere, reducing the oxygen availability near the front portion of the top sphere. Merging of the O_2 consumption zones is observed near the rear of the bottom 4 mm sphere in Fig. 12b.

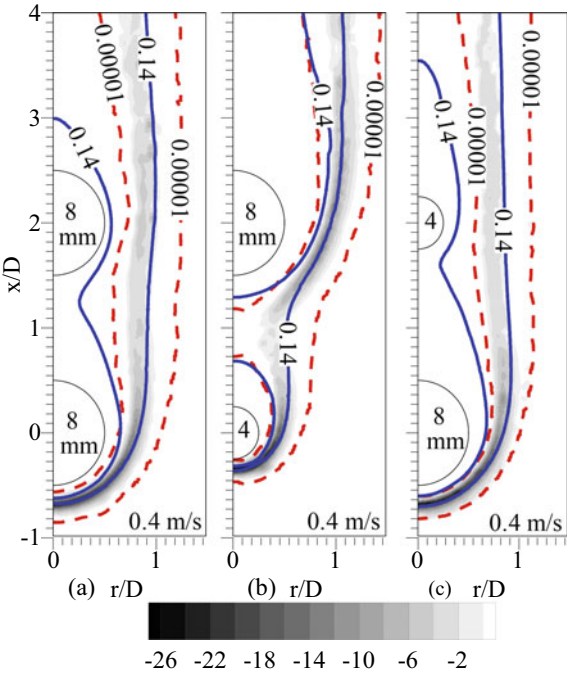

Fig. 12 Contours of net kinetic rate of O_2 (negative indicates consumption) with mass fraction lines of CO_2 (solid line) and OH (dash line) for air velocity of 0.4 m/s for the case of **a** 8 mm–8 mm, **b** 4 mm–8 mm, and **c** 8 mm–4 mm

In the wake regime, the net consumption rates of CH_3OH in kg/m^3-s (grayscale) for the three cases are portrayed in Fig. 13, at their respective critical velocities. Two-branched consumption zone of methanol, as discussed in the single sphere case, is observed, due to partial premixing occurring in the rear part of the bottom sphere in all the cases. The mass fraction contour lines of 0.13 for H_2O and 0.00001 for OH are seen to branch out from the maximum fuel consumption zone. Individual reaction zones are seen in the wake region of smaller bottom sphere and enveloping the 8 mm top sphere as in Fig. 13b. Merging of reaction zones of bottom and top spheres is seen in Fig. 13c for the 8 mm–4 mm configuration. OH mass fraction line of 0.00001 clearly bounds the maximum consumption and the outer branch of methanol consumption.

4 Conclusions

Heterogeneous methanol flames over porous sphere surfaces are simulated in Ansys Fluent in the laminar mixed convection regime. Fuel vaporization using interface boundary conditions is predicted using a user-defined function. A short reaction mechanism, (18 species and 38 elementary reactions) is incorporated to model the

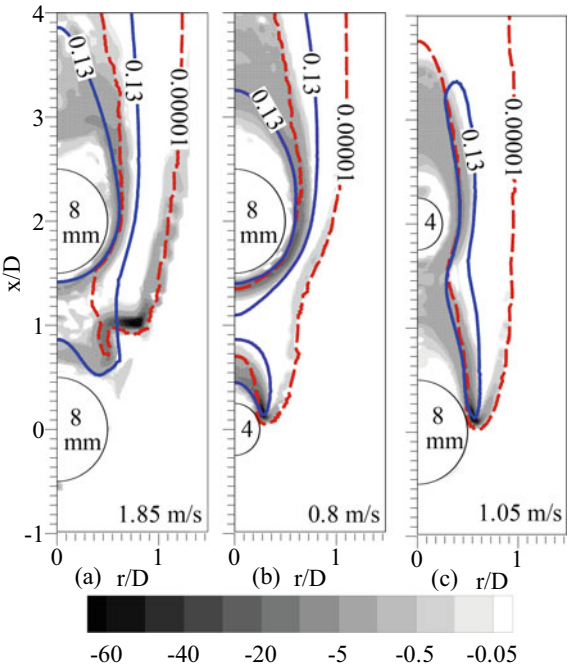

Fig. 13 Contours of net consumption rate of CH_3OH with mass fraction lines of H_2O (solid line) and OH (dash line) at critical velocity for the case of **a** 8 mm–8 mm, **b** 4 mm–8 mm, and **c** 8 mm–4 mm

kinetics. An optically thin radiation model accounts for the radiation losses of the participating species.

Two regimes of burning, dependent on sphere diameter and free stream velocity, are predicted by the model close to experimental data from literature at appropriate air velocities. Values of mass burning rates and its increase with an increase in the air velocity has been predicted quite reasonably by the model. Causation for this trend in terms of movement of stoichiometric contour line has been discussed. Critical velocity of flame transition from front part of the sphere to its rear part has been predicted reasonably closer to the experimental value for a single sphere case. In this case, the reactant mixture moves toward the rear portion of the sphere to form a partially premixed reaction zone in addition to the non-premixed flame zone. Branched reaction zones of methanol have been illustrated in the wake flame regime. There is a rapid reduction in the mass loss rate due to the absence of the flame in the front half of the porous sphere.

In the case of burning of two porous spheres in tandem arrangement, the resultant flow field as prescribed by the interaction between the two spheres, plays an important role in the determining the oxygen availability, especially for the sphere in the wake region, apart from dictating the overall flow field around both the spheres. The interference effects of the convective burning of two spheres and the resultant flame characteristics have been discussed with evidence of flow, temperature, species, and reaction fields, and compared with those of a single sphere. In the case where the bottom porous sphere shadows the top sphere from the incoming flow, especially

when the bottom sphere has a same or bigger diameter, oxygen deficiency is observed near the front half of the top porous sphere, resulting in lower mass burning rate. The values for the mass burning rates of the top sphere in this case are seen to be of the same order as that for a single porous sphere burning in the wake regime. Individual envelope flames for each of the spheres are not seen in this case and a single flame front forms.

The critical velocity of transition from envelope to wake flame is dependent on the arrangement of the two porous spheres and their interaction. When a wake flame is formed for the bottom sphere, its mass burning rate reduces drastically. Partial premixing in the rear half of the bottom sphere is observed. However, the mass burning rate for the top sphere increases due to the availability of oxygen and the presence of high temperature zone near its front part. The consumption zones of fuel and oxygen and production of CO_2 and H_2O through intermediates such as OH have been depicted for the different configurations. With the help of temperature, flow, species, and reaction fields, interpretations of the physical phenomena, which affect the flame structure and mass burning characteristics, have been explained.

Acknowledgements The authors thank P.G. Senapathy Center, IIT Madras for providing computing resources.

References

1. Spalding DB (1953) The combustion of liquid fuels. Symp (Int) Combust 4:847–864
2. Sami H, Ogasawara M (1970) Study on the burning of a fuel drop in heated and pressurized air stream: 1st report, experiment. Bull JSME 13(57):395–404
3. Gollahalli SR, Brzustowski TA (1973) "Experimental studies on the flame structure in the wake of a burning droplet. Symp (Int) Combust Combust Inst 14(1):1333–1344
4. König J, Eigenbrod C, Tanabe M, Renken H, Rath HJ (1996) Characterization of spherical hydrocarbon fuel flames: laser diagnosis of the chemical structure through the OH radical. Symp (Int) Combust 26(1):1235–1242
5. Balakrishnan P, Sundararajan T, Natarajan R (2001) Combustion of a fuel droplet in a mixed convective environment. Combust Sci Technol 163(1):77–106
6. Raghavan V, Babu V, Sundararajan T, Natarajan R (2005) Flame shapes and burning rates of spherical fuel particles in a mixed convective environment. Int J Heat Mass Transf 48(25–26):5354–5370
7. Das M, Chakraborty A, Datta A, Santra AK (2017) Experimental studies on burning characteristics of methanol, diesel, and sunflower biodiesel fuels. Combust Sci Technol 189(2):213–230
8. Tarrazo EF, Sanz MS, Sánchez AL, Williams FA (2016) A multipurpose reduced chemical-kinetic mechanism for methanol combustion. Combust Theor Model 20(4):613–631
9. Nair S, Raghavan V (2019) Numerical study of methanol flames in laminar forced convective environment using short chemical kinetics mechanism. Combust Theory Model 24(2):279–306

10. Barlow RS, Karpetis AN, Frank JH, Chen JY (2001) Scalar profiles and NO formation in laminar opposed-flow partially premixed methane/air flames. Combust Flame 127(3):2102–2118
11. Marchese AJ, Dryer FL (1997) The effect of non-luminous thermal radiation in microgravity droplet combustion. Combust Sci Technol 124(1–6):371–402
12. Dortmund Data Bank (DDBST GmbH) http://ddbonline.ddbst.com/AntoineCalculation/AntoineCalculationCGI.exe?component=Methanol